
Hyperbolic Geometry in Computer Vision: A Novel Framework for Convolutional Neural Networks

Ahmad Bdeir* **Kristian Schwethelm*** **Niels Landwehr**
 Data Science Department, University of Hildesheim
 {bdeira, schwethelm, landwehr}@uni-hildesheim.de

Abstract

Real-world visual data exhibit intrinsic hierarchical structures that can be represented effectively in hyperbolic spaces. Hyperbolic neural networks (HNNs) are a promising approach for learning feature representations in such spaces. However, current HNNs in computer vision rely on Euclidean backbones and only project features to the hyperbolic space in the task heads, limiting their ability to fully leverage the benefits of hyperbolic geometry. To address this, we present HCNN, the first fully hyperbolic convolutional neural network (CNN) designed for computer vision tasks. Based on the Lorentz model, we generalize fundamental components of CNNs and propose novel formulations of the convolutional layer, batch normalization, and multinomial logistic regression. Experimentation on standard vision tasks demonstrates the superiority of our HCNN framework and the Lorentz model in both hybrid and fully hyperbolic settings. Overall, we believe our contributions provide a foundation for developing more powerful HNNs that can better represent complex structures found in image data. Our code is publicly available at <https://github.com/kschwethelm/HyperbolicCV>.

1 Introduction

Representation learning is a fundamental aspect of deep neural networks, as obtaining an optimal representation of the input data is crucial. While Euclidean geometry has been the traditional choice for representing data due to its intuitive properties and well-defined vector space, recent research has highlighted the advantages of hyperbolic geometry in describing hierarchical structures found in many datasets. Specifically, hyperbolic manifolds allow for distances to scale exponentially with respect to the radius, which matches the exponential scaling of tree distances between hierarchy nodes, preventing spatial distortion and information loss [47]. In addition, research has found that even the natural spatial representations in the human brain exhibit a hyperbolic geometry [53].

Leveraging this better representative capacity, hyperbolic neural networks (HNNs) have demonstrated superior performance compared to Euclidean models in many natural language processing (NLP) and graph embedding tasks [42]. However, hierarchical structures are not limited to textual and graph-structured data but can also be found in images. The notion of hierarchy in images is particularly established through the concept of part-whole relationships within object representations and classes. In addition, Khrulkov et al. [22] have found high hyperbolicity in image datasets, where the hyperbolicity measure represents the degree of innate hierarchy between semantic embeddings and can highlight the potential benefits of using HNNs for representation learning.

In light of these findings, recent works have begun integrating hyperbolic geometry into vision architectures. Specifically, they rely on the Poincaré ball and the Lorentz model as descriptors of hyperbolic space and formalize hyperbolic translations of neural network layers. This is challenging due to ill-defined hyperbolic analogs of, e.g., addition, multiplication, and statistical measures.

*denotes equal contribution

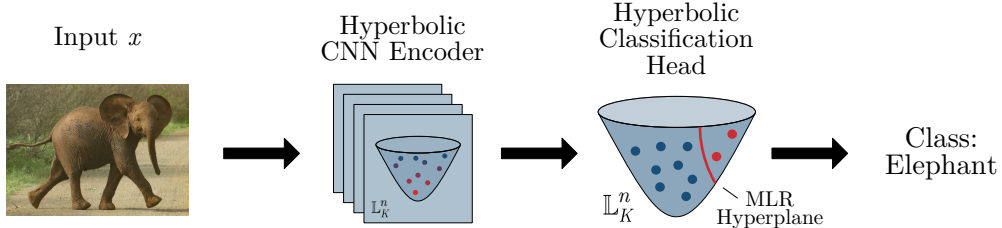


Figure 1: In contrast to hybrid HNNs that use a Euclidean CNN for feature extraction, our HCNN learns features in hyperbolic spaces in every layer, fully leveraging the benefits of hyperbolic geometry. This leads to better image representations and performance.

Currently, most HNN components are only available in the Poincaré ball as it supports the gyrovector space with basic vector operations. However, due to its hard numerical constraint, the Poincaré ball is more susceptible to numerical instability than the Lorentz model [36], which motivates introducing the missing layers for the Lorentz model. Moreover, HNNs in computer vision have been limited to hybrid architectures that can not fully leverage the advantages of hyperbolic geometry as they rely on Euclidean backbones to learn hyperbolic representations. Until now, fully hyperbolic architectures are missing in computer vision, although prevalent in NLP and graph applications [42].

In this work, we present HCNN, the first fully hyperbolic framework for vision tasks. We generalize the ubiquitous convolutional neural network (CNN) architecture to the Lorentz model and present novel hyperbolic formulations of the convolutional layer, batch normalization, and multinomial logistic regression. Our methodology is general, and we show that our components can be easily integrated into existing architectures. This is done through experiments based on direct translations of Euclidean architectures. Our contributions then become three-fold:

1. We propose the first fully hyperbolic CNN for image data, dubbed HCNN, introducing the fully hyperbolic setting in computer vision.
2. We provide missing Lorentzian formulations of the convolutional layer, batch normalization, and multinomial logistic regression, further filling the gap between HNNs in the Lorentz model and the Poincaré ball.
3. We empirically demonstrate the superior performance of HCNNs in experiments on standard vision tasks, including image classification and generation.

2 Related work

Hyperbolic image embeddings Previous research on HNNs in computer vision has mainly focused on combining Euclidean backbones and hyperbolic embeddings. This approach involves projecting Euclidean embeddings onto the hyperbolic space in the task heads and designing task-related objective functions based on hyperbolic geometry. Such simple hybrid architectures have been proven effective in various vision tasks like recognition [16, 22, 31], segmentation [1, 20], reconstruction/generation [35, 38, 40, 44], and metric learning [10, 51]. However, Guo et al. [16] have shown that learning a mixture of Euclidean and hyperbolic features can exacerbate gradient vanishing, and it remains unclear whether these hybrid models can fully exploit the properties of hyperbolic geometry. In contrast, our HCNN naturally learns latent hyperbolic feature representations in every layer, mitigating these issues. We also forgo the typically used Poincaré ball in favor of the Lorentz model, as it offers better stability and optimization properties [36].

Fully hyperbolic neural networks Designing fully hyperbolic HNNs requires generalizing all Euclidean network components to hyperbolic geometry. Notably, Ganea et al. [12] and Shimizu et al. [49] utilized the Poincaré ball and the gyrovector space to generalize various layers, including fully-connected, convolutional, and attention layers, as well as operations like split, concatenation, and multinomial logistic regression (MLR). Researchers have also designed components in the Lorentz model [5, 11, 39, 44], but crucial components for vision, like the standard convolutional layer and the MLR classifier, are still missing. Among the hyperbolic layer definitions, fully hyperbolic neural networks have been built for various tasks in NLP and graph applications [42]. However, no fully

hyperbolic architecture has yet been utilized in computer vision. Our work provides formulations for missing components in the Lorentz model, allowing for the first fully hyperbolic vision CNNs.

Normalization in HNNs There are few attempts at translating standard normalization layers to the hyperbolic setting. To the best of our knowledge, there is only a single viable normalization layer for HNNs, i.e., the general Riemannian batch normalization [33]. However, this method is not ideal due to the slow iterative computation of the Fréchet mean and the arbitrary re-scaling operation that is not based on hyperbolic geometry. In this work, we propose an efficient batch normalization algorithm founded in the Lorentz model, which utilizes the Lorentzian centroid [27] and a mathematically motivated re-scaling operation.

Numerical stability of HNNs The exponential growth of the Lorentz model’s volume with respect to the radius can introduce numerical instability and rounding errors in floating-point arithmetic. This requires many works to rely on 64-bit precision at the cost of higher memory and runtime requirements. To mitigate this, researchers have introduced feature clipping and Euclidean reparameterizations [16, 35, 36]. We adopt these approaches in HCNN, allowing us to run under 32-bit floating point arithmetic, reducing the computational cost.

3 Background

This section summarizes the mathematical background of hyperbolic geometry [3, 45]. The n -dimensional hyperbolic space \mathbb{H}_K^n is a smooth Riemannian manifold $(\mathcal{M}^n, \mathbf{g}_x^K)$ with constant negative curvature $K < 0$, where \mathcal{M}^n and \mathbf{g}_x^K represent the manifold and the Riemannian metric, respectively. There are multiple isometrically equivalent models of hyperbolic geometry. We employ the Lorentz model because of its numerical stability and its simple exponential/logarithmic maps and distance functions. Additionally, we use the Poincaré ball for baseline implementations. Both hyperbolic models provide closed-form formulae for manifold operations, including distance measures, exponential/logarithmic maps, and parallel transportation. They are detailed in Appendix A.

Lorentz model The n -dimensional Lorentz model $\mathbb{L}_K^n = (\mathcal{L}^n, \mathbf{g}_x^K)$ models hyperbolic geometry on the upper sheet of a two-sheeted hyperboloid \mathcal{L}^n , with origin $\bar{\mathbf{0}} = [\sqrt{-1/K}, 0, \dots, 0]^T$ and embedded in $(n+1)$ -dimensional Minkowski space (see Figure 2). Based on the Riemannian metric $\mathbf{g}_x^K = \text{diag}(-1, 1, \dots, 1)$, the manifold is defined as

$$\mathcal{L}^n := \{\mathbf{x} \in \mathbb{R}^{n+1} \mid \langle \mathbf{x}, \mathbf{x} \rangle_{\mathcal{L}} = \frac{1}{K}, x_t > 0\}, \quad (1)$$

with the Lorentzian inner product

$$\langle \mathbf{x}, \mathbf{y} \rangle_{\mathcal{L}} := -x_t y_t + \mathbf{x}_s^T \mathbf{y}_s = \mathbf{x}^T \text{diag}(-1, 1, \dots, 1) \mathbf{y}. \quad (2)$$

When describing points in the Lorentz model, we inherit the terminology of special relativity and call the first dimension the *time component* x_t and the remaining dimensions the *space component* \mathbf{x}_s , such that $\mathbf{x} \in \mathbb{L}_K^n = [x_t, \mathbf{x}_s]^T$ and $x_t = \sqrt{\|\mathbf{x}_s\|^2 - 1/K}$.

Poincaré ball The n -dimensional Poincaré ball $\mathbb{B}_K^n = (\mathcal{B}^n, \mathbf{g}_x^K)$ is defined by $\mathcal{B}^n = \{\mathbf{x} \in \mathbb{R}^n \mid -K\|\mathbf{x}\|^2 < 1\}$ and the Riemannian metric $\mathbf{g}_x^K = (\lambda_x^K)^2 \mathbf{I}_n$, where $\lambda_x^K = 2(1 + K\|\mathbf{x}\|^2)^{-1}$. It describes the hyperbolic space by an open ball of radius $\sqrt{-1/K}$, see Figure 2.

4 Fully hyperbolic CNN (HCNN)

Our HCNN framework aims to give way to building vision models that can fully leverage the advantages of hyperbolic geometry by learning features in hyperbolic spaces. For this, we generalize Euclidean CNN components to the Lorentz model, yielding one-to-one replacements that can be integrated into existing architectures. In the following, we first define the cornerstone of HCNNs, i.e., the Lorentz convolutional layer, including its transposed variant. Then, we introduce the Lorentz batch normalization algorithm and the MLR classifier. Finally, we generalize the residual connection and non-linear activation.

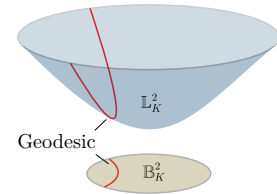


Figure 2: Comparison of Lorentz and Poincaré model.

4.1 Lorentz convolutional layer

Hyperbolic feature maps The convolutional layer applies vector operations to an input feature map containing the activations of the previous layer. In Euclidean space, arbitrary numerical values can be combined to form a vector. Therefore, it is not required to strictly determine which feature map dimension holds feature vectors. However, in the Lorentz model, not all possible value combinations represent a point that can be processed with hyperbolic operations ($\mathbb{L}_K^n \subset \mathbb{R}^{n+1}$).

We propose using channel-last feature map representations throughout HCNNs and adding the Lorentz model’s time component as an additional channel dimension. This defines a hyperbolic feature map as an ordered set of n -dimensional hyperbolic vectors, where every spatial position contains a vector that can be combined with its neighbors. Additionally, it offers a nice interpretation where an image is an ordered set of color vectors, each describing a pixel.

Formalization of the convolutional layer We define the convolutional layer as an affine transformation between a linearized kernel and a concatenation of the values in its receptive field, following Shimizu et al. [49]. Then, we generalize this definition by replacing the Euclidean operators with their hyperbolic counterparts in the Lorentz model.

Given a hyperbolic input feature map $\mathbf{x} = \{\mathbf{x}_{h,w} \in \mathbb{L}_K^n\}_{h,w=1}^{H,W}$ as an ordered set of n -dimensional hyperbolic feature vectors, each describing image pixels, the features within the receptive field of the kernel $\mathbf{K} \in \mathbb{R}^{m \times n \times \tilde{H} \times \tilde{W}}$ are $\{\mathbf{x}_{h'+\delta\tilde{h}, w'+\delta\tilde{w}} \in \mathbb{L}_K^n\}_{\tilde{h}, \tilde{w}=1}^{\tilde{H}, \tilde{W}}$, where (h', w') denotes the starting position and δ is the stride parameter. Now, we define the Lorentz convolutional layer as

$$\mathbf{y}_{h,w} = \text{LFC}(\text{HCat}(\{\mathbf{x}_{h'+\delta\tilde{h}, w'+\delta\tilde{w}} \in \mathbb{L}_K^n\}_{\tilde{h}, \tilde{w}=1}^{\tilde{H}, \tilde{W}})), \quad (3)$$

where HCat denotes the concatenation of hyperbolic vectors, and LFC denotes a Lorentz fully-connected layer performing the affine transformation and parameterizing the kernel and bias, respectively. Additionally, we implement padding using origin vectors, the analog of zero vectors in hyperbolic space.

Finally, our formulation generalizes arbitrary dimensional convolutional layers with little modification to the 2-dimensional case presented here. However, it remains essential to predetermine the structure of hyperbolic feature maps, e.g., using our channel-last format.

Extension to the transposed setting The transposed convolutional layer is usually used in encoder-decoder architectures for up-sampling. Given a hyperbolic convolutional layer, it is straightforward to generalize to hyperbolic space. A convolutional layer carries out a transposed convolution when the correct local connectivity is established by inserting zeros at certain positions. Specifically, when stride $s > 1$, then $s - 1$ zero vectors are inserted between the features. In addition, the input feature map is always implicitly padded on each side. We refer to Dumoulin and Visin [9] for illustrations. Under this relationship, the Lorentz transposed convolutional layer is a Lorentz convolutional layer with changed connectivity through origin padding.

4.2 Lorentz batch normalization

Given a batch \mathcal{B} of m features \mathbf{x}_i , the traditional batch normalization algorithm [21] calculates the mean $\mu_{\mathcal{B}} = \frac{1}{m} \sum_{i=1}^m \mathbf{x}_i$ and variance $\sigma_{\mathcal{B}}^2 = \frac{1}{m} \sum_{i=1}^m (\mathbf{x}_i - \mu_{\mathcal{B}})^2$ across the batch dimension. Then, the features are *re-scaled* and *re-centered* using a parameterized variance γ and mean β as follows

$$\text{BN}(\mathbf{x}_i) = \gamma \odot \frac{\mathbf{x}_i - \mu_{\mathcal{B}}}{\sqrt{\sigma_{\mathcal{B}}^2 + \epsilon}} + \beta. \quad (4)$$

At test time, running estimates approximate the batch statistics. They are calculated iteratively during training: $\mu_t = (1 - \eta)\mu_{t-1} + \eta\mu_{\mathcal{B}}$ and $\sigma_t^2 = (1 - \eta)\sigma_{t-1}^2 + \eta\sigma_{\mathcal{B}}^2$, with η and t denoting momentum and the current iteration, respectively. We generalize batch normalization to the Lorentz model using the Lorentzian centroid and the parallel transport operation for re-centering, and the Fréchet variance and straight geodesics at the origin’s tangent space for re-scaling.

Re-centering To re-center hyperbolic features, it is necessary to compute a notion of mean. Usually, the Fréchet mean is used [33], which minimizes the expected squared distance between a set of points in a metric space [43]. Generally, the Fréchet mean must be solved iteratively, massively slowing down training. To this end, we propose to use the centroid with respect to the squared Lorentzian distance, which can be calculated efficiently in closed form [27]. The weighted Lorentzian centroid, which solves $\min_{\mu \in \mathbb{L}_K^n} \sum_{i=1}^m \nu_i d_{\mathcal{L}}^2(\mathbf{x}_i, \mu)$, with $\mathbf{x}_i \in \mathbb{L}_K^n$ and $\nu_i \geq 0$, $\sum_{i=1}^m \nu_i > 0$, is given by

$$\mu = \frac{\sum_{i=1}^m \nu_i \mathbf{x}_i}{\sqrt{-K} \|\sum_{i=1}^m \nu_i \mathbf{x}_i\|_{\mathcal{L}}}. \quad (5)$$

In batch normalization, the mean is not weighted, which gives $\nu_i = \frac{1}{m}$. Now, we shift the features from the batch's mean μ_B to the parameterized mean β using the parallel transport operation $\text{PT}_{\mu_B \rightarrow \beta}^K(\mathbf{x})$. Parallel transport does not change the variance, as it is defined to preserve the distance between all points. Finally, the running estimate is updated iteratively using the weighted centroid with $\nu_1 = (1 - \eta)$ and $\nu_2 = \eta$.

Re-scaling For re-scaling, we rely on the Fréchet variance $\sigma^2 \in \mathbb{R}^+$, defined as the expected squared Lorentzian distance between a point \mathbf{x}_i and the mean μ , and given by $\sigma^2 = \frac{1}{m} \sum_{i=1}^m d_{\mathcal{L}}^2(\mathbf{x}_i, \mu)$ [24]. In order to re-scale the batch, features must be moved along the geodesics connecting them to their centroid, which is generally infeasible to compute. However, geodesics intersecting the origin are very simple, as they can be represented by straight lines in tangent space $\mathcal{T}_{\bar{0}} \mathbb{L}_K^n$. This is reflected by the equality between the distance of a point to the origin and the length of its corresponding tangent vector ($d_{\mathcal{L}}(\mathbf{x}, \bar{0}) = \|\log_{\bar{0}}^K(\mathbf{x})\|$). Using this property, we propose to re-scale features by first parallel transporting them towards the origin $\text{PT}_{\mu_B \rightarrow \bar{0}}^K(\mathbf{x})$, making the origin the new centroid and straightening the relevant geodesics. Then, a simple multiplication re-scales the features in tangent space. Finally, parallel transporting to $\beta \in \mathbb{L}_K^n$ completes the algorithm and yields the normalized features. The final algorithm of Lorentz batch normalization can be formalized as

$$\text{LBN}(\mathbf{x}) = \exp_{\beta}^K \left(\text{PT}_{\bar{0} \rightarrow \beta}^K \left(\gamma \cdot \frac{\text{PT}_{\mu_B \rightarrow \bar{0}}^K(\log_{\mu_B}^K(\mathbf{x}))}{\sqrt{\sigma_B^2} + \epsilon} \right) \right). \quad (6)$$

In our definition of hyperbolic feature maps, the centroid must be computed across multiple dimensions. For example, given a feature map $\{\mathbf{x}_{h,w} \in \mathbb{L}_K^n\}_{h,w=1}^{H,W}$ for all m instances, we first compute the centroid of all hyperbolic vectors per instance and then the centroid across the batch dimension, i.e., the centroid of instance centroids. Similarly, the Fréchet variance is computed for separate instances and then averaged across the batch dimension as it is in \mathbb{R}^+ . Furthermore, the running estimate of the Fréchet variance is computed using a standard Euclidean running average.

4.3 Lorentz MLR classifier

In this section, we consider the problem of classifying instances that are represented in the Lorentz model. A standard method for multi-class classification is multinomial logistic regression (MLR). Inspired by the generalization of MLR to the Poincaré ball [12, 49] based on the distance to margin hyperplanes, we derive a formulation in the Lorentz model.

Hyperplane in the Lorentz model Analogous to Euclidean space, hyperbolic hyperplanes split the manifold into two half-spaces, which can then be used to separate instances into classes. The hyperplane in the Lorentz model is defined by a geodesic that results from the intersection of an n -dimensional hyperplane with the hyperboloid in the ambient space \mathbb{R}^{n+1} [6]. Specifically, for $\mathbf{p} \in \mathbb{L}_K^n$ and $\mathbf{w} \in \mathcal{T}_{\mathbf{p}} \mathbb{L}_K^n$, the hyperplane passing through \mathbf{p} and perpendicular to \mathbf{w} is given by

$$H_{\mathbf{w}, \mathbf{p}} = \{\mathbf{x} \in \mathbb{L}_K^n \mid \langle \mathbf{w}, \mathbf{x} \rangle_{\mathcal{L}} = 0\}. \quad (7)$$

This formulation comes with the non-convex optimization condition $\langle \mathbf{w}, \mathbf{w} \rangle_{\mathcal{L}} > 0$, which is undesirable in machine learning. To eliminate this condition, we use the Euclidean reparameterization

of Mishne et al. [36], which we extend to include the curvature parameter K in Appendix B.1. In short, \mathbf{w} is parameterized by a vector $\bar{\mathbf{z}} \in \mathcal{T}_{\bar{\mathbf{0}}} \mathbb{L}_K^n = [0, a\mathbf{z}/\|\mathbf{z}\|]$, where $a \in \mathbb{R}$ and $\mathbf{z} \in \mathbb{R}^n$. As $\mathbf{w} \in \mathcal{T}_{\mathbf{p}} \mathbb{L}_K^n$, $\bar{\mathbf{z}}$ is parallel transported to \mathbf{p} , which gives

$$\mathbf{w} := \text{PT}_{\bar{\mathbf{0}} \rightarrow \mathbf{p}}^K(\bar{\mathbf{z}}) = [\sinh(\sqrt{-K}a)\|\mathbf{z}\|, \cosh(\sqrt{-K}a)\mathbf{z}]. \quad (8)$$

Inserting Eq. 8 into Eq. 7, the formula of the Lorentz hyperplane becomes

$$\tilde{H}_{\mathbf{z},a} = \{\mathbf{x} \in \mathbb{L}_K^n \mid \cosh(\sqrt{-K}a)\langle \mathbf{z}, \mathbf{x}_s \rangle - \sinh(\sqrt{-K}a)\|\mathbf{z}\|x_t = 0\}, \quad (9)$$

where a and \mathbf{z} represent the distance and orientation to the origin, respectively.

Finally, we need the distance to the hyperplane to quantify the model's confidence. It is formulated by the following theorem, proven in Appendix B.2.

Theorem 1 *Given $a \in \mathbb{R}$ and $\mathbf{z} \in \mathbb{R}^n$, the minimum hyperbolic distance from a point $\mathbf{x} \in \mathbb{L}_K^n$ to the hyperplane $\tilde{H}_{\mathbf{z},a}$ defined in Eq. 9 is given by*

$$d_{\mathcal{L}}(\mathbf{x}, \tilde{H}_{\mathbf{z},a}) = \frac{1}{\sqrt{-K}} \left| \sinh^{-1} \left(\sqrt{-K} \frac{\cosh(\sqrt{-K}a)\langle \mathbf{z}, \mathbf{x}_s \rangle - \sinh(\sqrt{-K}a)\|\mathbf{z}\|x_t}{\sqrt{\|\cosh(\sqrt{-K}a)\mathbf{z}\|^2 - (\sinh(\sqrt{-K}a)\|\mathbf{z}\|)^2}} \right) \right|. \quad (10)$$

MLR in the Lorentz model Lebanon and Lafferty [29] formulated the logits of the Euclidean MLR classifier using the distance from instances to hyperplanes describing the class regions. Specifically, given input $\mathbf{x} \in \mathbb{R}^n$ and C classes, the output probability of class $c \in \{1, \dots, C\}$ can be expressed as

$$p(y = c \mid \mathbf{x}) \propto \exp(v_{\mathbf{w}_c}(\mathbf{x})), \quad v_{\mathbf{w}_c}(\mathbf{x}) = \text{sign}(\langle \mathbf{w}_c, \mathbf{x} \rangle) \|\mathbf{w}_c\| d(\mathbf{x}, H_{\mathbf{w}_c}), \quad \mathbf{w}_c \in \mathbb{R}^n, \quad (11)$$

where $H_{\mathbf{w}_c}$ is the decision hyperplane of class c .

We define the Lorentz MLR without loss of generality by inserting the Lorentzian counterparts into Eq. 11. This yields logits given by the following theorem, proven in Appendix B.3.

Theorem 2 *Given parameters $a_c \in \mathbb{R}$ and $\mathbf{z}_c \in \mathbb{R}^n$, the Lorentz MLR's output logit corresponding to class c and input $\mathbf{x} \in \mathbb{L}_K^n$ is given by*

$$v_{\mathbf{z}_c, a_c}(\mathbf{x}) = \frac{1}{\sqrt{-K}} \text{sign}(\alpha) \beta \left| \sinh^{-1} \left(\sqrt{-K} \frac{\alpha}{\beta} \right) \right|, \quad (12)$$

with

$$\begin{aligned} \alpha &= \cosh(\sqrt{-K}a)\langle \mathbf{z}, \mathbf{x}_s \rangle - \sinh(\sqrt{-K}a), \\ \beta &= \sqrt{\|\cosh(\sqrt{-K}a)\mathbf{z}\|^2 - (\sinh(\sqrt{-K}a)\|\mathbf{z}\|)^2}. \end{aligned}$$

4.4 Lorentz residual connection and activation

Residual connection The residual connection is a crucial component when designing deep CNNs. As vector addition is ill-defined in the Lorentz model, we add the vector's space components and concatenate a corresponding time component. This is possible as a point $\mathbf{x} \in \mathbb{L}_K^n$ can be defined by an arbitrary space component $\mathbf{x}_s \in \mathbb{R}^n$ and a time component $x_t = \sqrt{\|\mathbf{x}_s\|^2 - 1/K}$. Our method is straightforward and provides the best empirical performance compared to other viable methods for addition we implemented, i.e., tangent space addition [39], parallel transport addition [4], Möbius addition (after projecting to the Poincaré ball) [12], and fully-connected layer addition [5].

Non-linear activation Prior works use non-linear activation in tangent space [11], which weakens the model’s stability due to frequent logarithmic and exponential maps. We propose to simplify the operation for the Lorentz model by applying the activation function to the space component and concatenating a time component. For example, the Lorentz ReLU activation is given by

$$\mathbf{y} = \begin{bmatrix} \sqrt{\|\text{ReLU}(\mathbf{x}_s)\|^2 - 1/K} \\ \text{ReLU}(\mathbf{x}_s) \end{bmatrix}. \quad (13)$$

This operation can be interpreted similarly to Euclidean activations that break linearity with heuristic mathematical projections.

5 Experiments

We evaluate HCNN models on image classification and generation tasks and compare them against Euclidean and hybrid HNN counterparts. To ensure a fair comparison, in every task, we directly translate a Euclidean baseline to the hyperbolic setting by using hyperbolic modules as one-to-one replacements. All experiments are implemented in PyTorch [41], and we optimize hyperbolic models using adaptive Riemannian optimizers [2] provided by Geoopt [25], with floating-point precision set to 32 bits. We provide detailed experimental configurations in Appendix C and many ablation experiments in Appendix D. To facilitate reproducibility and further exploration, we make the code of our experiments publicly available at <https://github.com/kschwethelm/HyperbolicCV..>

5.1 Image classification

Experimental setup In this experiment, we evaluate the performance of HCNN on standard image classification tasks using ResNet-18 [18] and three benchmark datasets: CIFAR-10 [26], CIFAR-100 [26], and Tiny-ImageNet [28]. We compare against the Euclidean network by replacing all components in the ResNet architecture with our proposed Lorentzian modules. Establishing hyperbolic baselines is difficult, as there are currently no fully hyperbolic models for vision tasks, and only hybrid models with task-specific output layers that largely do not apply to standard classification [10, 22, 31, 50]. Specifically, current vision HNNs use Euclidean CNNs for embedding images, project the final embeddings onto hyperbolic space, and only apply a hyperbolic output layer. This leaves us with a single viable hyperbolic baseline from the literature: Following Atigh et al. [1] and Guo et al. [16], we implement the hybrid approach with the Poincaré MLR classifier [49]. In addition, however, we utilize our proposed Lorentz MLR to obtain a novel hybrid baseline that uses the Lorentz model instead of the Poincaré ball. Finally, we apply feature clipping on embeddings of both hybrid models to prevent gradient issues arising from the hybrid architecture [16].

For all models, we adopt DeVries and Taylor’s [8] training procedure and hyperparameters, which have been optimized for Euclidean CNNs and yield a strong Euclidean ResNet baseline. For example, this method increases CIFAR-100 performance from 74.84% for the original ResNet-110 [52] to 77.72% we obtained for the much smaller ResNet-18. To make a rigorous one-to-one comparison, we do not optimize the training procedure and hyperparameters for the hyperbolic models but keep the settings of [8]. This suggests that HNN performance can still be improved.

Main results The results in Table 1 show that our fully hyperbolic ResNet achieves the highest accuracy on all datasets, outperforming both Euclidean and hybrid baselines. Additionally, our novel hybrid HNN based on the Lorentz model performs well, outperforming the Euclidean model on two datasets. In contrast, the hybrid Poincaré HNN is inferior to the Euclidean baseline, which is consistent with the results reported by Guo et al. [16]. This suggests that the Lorentz model is better suited for HNNs than the Poincaré ball. Overall, our results highlight the potential of our HCNN components and the Lorentz model in improving image classification tasks.

Adversarial robustness Prior works have indicated that HNNs can obtain better adversarial robustness than Euclidean networks. To study this, we employ the models trained on CIFAR-100 and attack them using FGSM [14] and PGD [34] with a maximal perturbation of $\epsilon = 0.8/255, 1.6/255, 3.2/255$. The results in Table 2 show that our HCNN is much more robust than the other models, getting up to 5% higher accuracy. In addition, contrary to Guo et al. [16], we observe that hybrid HNNs are more susceptible to adversarial attacks than Euclidean models.

Table 1: Classification accuracy (%) of ResNet-18 models. We estimate the mean and standard deviation from five runs. The best performance is highlighted in bold (higher is better).

	CIFAR-10	CIFAR-100	Tiny-ImageNet
Euclidean [18]	95.14 ± 0.12	77.72 ± 0.15	65.19 ± 0.12
Hybrid Poincaré [1, 16]	95.04 ± 0.13	77.19 ± 0.50	64.93 ± 0.38
Hybrid Lorentz (Ours)	94.98 ± 0.12	78.03 ± 0.21	65.63 ± 0.10
HCNN Lorentz (Ours)	95.14 ± 0.08	78.07 ± 0.17	65.71 ± 0.13

Table 2: Classification accuracy (%) after performing FGSM and PGD attacks on CIFAR-100. We estimate the mean and standard deviation from attacking five trained models. The best performance is highlighted in bold (higher is better).

Max. perturbation ϵ	FGSM			PGD		
	0.8/255	1.6/255	3.2/255	0.8/255	1.6/255	3.2/255
Euclidean [18]	65.70 ± 0.28	54.98 ± 0.39	39.97 ± 0.43	64.43 ± 0.29	49.76 ± 0.42	26.30 ± 0.40
Hybrid Poincaré [1, 16]	64.68 ± 0.40	53.32 ± 0.60	37.52 ± 0.50	63.43 ± 0.44	48.41 ± 0.60	23.78 ± 0.75
Hybrid Lorentz (Ours)	65.27 ± 0.52	53.82 ± 0.49	40.53 ± 0.31	64.15 ± 0.53	49.05 ± 0.68	27.17 ± 0.40
HCNN Lorentz (Ours)	66.47 ± 0.27	57.14 ± 0.30	43.51 ± 0.35	65.04 ± 0.28	52.25 ± 0.34	31.77 ± 0.55

Low embedding dimensionality HNNs have shown to be most effective in lower-dimensional spaces. To this end, we reduce the dimensionality of the final ResNet block and the embeddings and evaluate classification accuracy on CIFAR-100.

The results in Figure 3 verify the effectiveness of hyperbolic spaces with low dimensions, where all HNNs outperform the Euclidean models. However, our HCNN can leverage this advantage best, suggesting that HCNNs offer great opportunities for dimensionality reduction and designing smaller models with fewer parameters. This can be useful, e.g., in mobile deployment.

5.2 Image generation

Experimental setup Variational autoencoders (VAEs) [23, 46] have been widely adopted in HNN research to model latent embeddings in hyperbolic spaces [20, 35, 38, 40]. However, these works rely on hybrid architectures and mainly focus on learning strong embeddings rather than targeting image generation. In this experiment, we extend the hyperbolic VAE to the fully hyperbolic setting using our proposed HCNN framework and, for the first time, evaluate its performance on image generation using the standard Fréchet Inception Distance (FID) metric [19].

Building on the experimental setting of Ghosh et al. [13], we test vanilla VAEs and assess generative performance on CIFAR-10 [26], CIFAR-100 [26], and CelebA [32] datasets. We compare our HCNN-VAE against the Euclidean and two hybrid models. Following prior works, the hybrid models only include a latent hyperbolic distribution and no hyperbolic layers. Specifically, we employ the wrapped normal distributions in the Lorentz model [38] and the Poincaré ball [35], respectively.

Main results The results in Table 3 show that our HCNN-VAE outperforms all baselines. Likewise, the hybrid models improve performance over the Euclidean model, indicating that learning the latent embeddings in hyperbolic spaces is beneficial. However, our HCNN is better at leveraging the advantages of hyperbolic geometry due to its fully hyperbolic architecture. These results suggest that our method is a promising approach for generation and for modeling latent structures in image data.

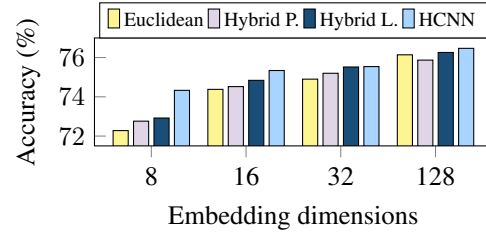


Figure 3: CIFAR-100 accuracy obtained with lower dimensionalities in the final ResNet block. The standard embedding dimension is $d_E = 512$.

Table 3: Reconstruction and generation FID of manifold VAEs. We estimate the mean and standard deviation from five runs. The best performance is highlighted in bold (lower is better).

	CIFAR-10		CIFAR-100		CelebA	
	Rec. FID	Gen. FID	Rec. FID	Gen. FID	Rec. FID	Gen. FID
Euclidean	61.21 ± 0.72	92.40 ± 0.80	63.81 ± 0.47	103.54 ± 0.84	54.80 ± 0.29	79.25 ± 0.89
Hybrid Poincaré [35]	59.85 ± 0.50	90.13 ± 0.77	62.64 ± 0.43	98.19 ± 0.57	54.62 ± 0.61	81.30 ± 0.56
Hybrid Lorentz [38]	59.29 ± 0.47	90.91 ± 0.84	62.14 ± 0.35	98.34 ± 0.62	54.64 ± 0.34	82.78 ± 0.93
HCNN Lorentz (Ours)	57.78 ± 0.56	89.20 ± 0.85	61.44 ± 0.64	100.27 ± 0.84	54.17 ± 0.66	78.11 ± 0.95

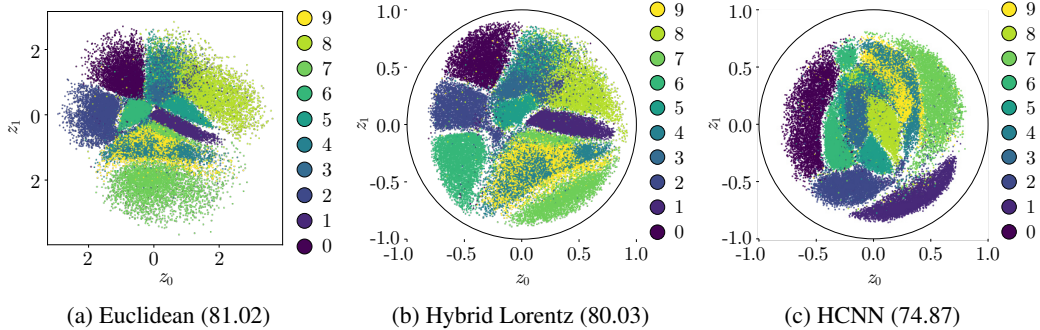


Figure 4: Embeddings of MNIST training data in 2D latent space of VAEs. Each embedding is represented by a point colored by the input’s ground truth label. The embeddings of Lorentz HNNs are projected onto the Poincaré ball for better visualization. Additionally, we give the generation FID.

Analysis of latent embeddings The latent embedding space is a crucial component of VAEs as it influences how the data’s features are encoded and used for generating the output. We visually analyze the distribution of latent embeddings inferred by the VAEs. For this, the models are retrained on the MNIST [30] dataset with an embedding dimension $d_E = 2$. Then, the images of the training dataset are passed through the encoder and visualized as shown in Figure 4.

We observe the formation of differently shaped clusters that correlate with the ground truth labels. While the embeddings of the Euclidean and hybrid models form many clusters that direct towards the origin, the HCNN-VAE obtains rather curved clusters that keep a similar distance to the origin. The structures within the HCNN’s latent space can be interpreted as hierarchies where the distance to the origin represents hierarchical levels. As these structures cannot be found for the hybrid model, our results suggest that hybrid HNNs behave more like Euclidean models than hyperbolic models and can not fully leverage the properties of the hyperbolic space, resulting in inferior performance.

6 Conclusion

In this work, we proposed HCNN, a generalization of the convolutional neural network that learns latent feature representations in hyperbolic spaces. To this end, we formalized the necessary modules in the Lorentz model, deriving novel formulations of the convolutional layer, batch normalization, and multinomial logistic regression. We empirically demonstrated that ResNet and VAE models based on our HCNN framework achieve better performance on standard vision tasks than Euclidean and hybrid baselines, especially in adversarial and lower dimensional settings. Additionally, we showed that using the Lorentz model in HNNs leads to better stability and performance than the Poincaré ball.

However, HCNNs are still in their early stages, and it remains to be seen to which extent they can replace Euclidean networks as they introduce mathematical complexity and computational overhead. Moreover, our HCNN framework relies on generalizations of neural network layers that were designed for Euclidean geometry and might not fully capture the unique properties of hyperbolic geometry. Further research is needed to fully understand the properties of HCNNs and address open questions such as optimization, scalability, and performance on other deep learning problems. We hope our work will inspire future research and development in this exciting and rapidly evolving field.

Acknowledgments and Disclosure of Funding

This work was performed on the HoreKa supercomputer funded by the Ministry of Science, Research and the Arts Baden-Württemberg and by the Federal Ministry of Education and Research. Ahmad Bdeir was funded by the European Union's Horizon 2020 research and innovation programme under the SustInAfrica grant agreement No 861924. Kristian Schwethelm was funded by the Deutsche Forschungsgemeinschaft (DFG, German Research Foundation) - project number 225197905.

References

- [1] M. G. Atigh, J. Schoep, E. Acar, N. van Noord, and P. Mettes. Hyperbolic image segmentation. In *Proceedings of the IEEE/CVF Conference on Computer Vision and Pattern Recognition (CVPR)*, pages 4453–4462, June 2022.
- [2] G. Bécigneul and O.-E. Ganea. Riemannian adaptive optimization methods, 2018. URL <https://arxiv.org/abs/1810.00760>.
- [3] J. W. Cannon, W. J. Floyd, R. Kenyon, and W. R. Parry. *Hyperbolic Geometry*, volume 31. MSRI Publications, 2006.
- [4] I. Chami, R. Ying, C. Ré, and J. Leskovec. Hyperbolic graph convolutional neural networks, 2019. URL <https://arxiv.org/abs/1910.12933>.
- [5] W. Chen, X. Han, Y. Lin, H. Zhao, Z. Liu, P. Li, M. Sun, and J. Zhou. Fully hyperbolic neural networks. *CoRR*, abs/2105.14686, 2021. URL <https://arxiv.org/abs/2105.14686>.
- [6] H. Cho, B. DeMeo, J. Peng, and B. Berger. Large-margin classification in hyperbolic space. In K. Chaudhuri and M. Sugiyama, editors, *Proceedings of the Twenty-Second International Conference on Artificial Intelligence and Statistics*, volume 89 of *Proceedings of Machine Learning Research*, pages 1832–1840. PMLR, 16–18 Apr 2019. URL <https://proceedings.mlr.press/v89/cho19a.html>.
- [7] J. Deng, W. Dong, R. Socher, L.-J. Li, K. Li, and L. Fei-Fei. Imagenet: A large-scale hierarchical image database. In *2009 IEEE Conference on Computer Vision and Pattern Recognition*, pages 248–255, 2009. doi: 10.1109/CVPR.2009.5206848.
- [8] T. DeVries and G. W. Taylor. Improved regularization of convolutional neural networks with cutout, 2017. URL <https://arxiv.org/abs/1708.04552>.
- [9] V. Dumoulin and F. Visin. A guide to convolution arithmetic for deep learning, 2016. URL <https://arxiv.org/abs/1603.07285>.
- [10] A. Ermolov, L. Mirvakhabova, V. Khrulkov, N. Sebe, and I. Oseledets. Hyperbolic vision transformers: Combining improvements in metric learning, 2022. URL <https://arxiv.org/abs/2203.10833>.
- [11] X. Fan, C.-H. Yang, and B. C. Vemuri. Nested hyperbolic spaces for dimensionality reduction and hyperbolic nn design. In *2022 IEEE/CVF Conference on Computer Vision and Pattern Recognition (CVPR)*, pages 356–365, 2022. doi: 10.1109/CVPR52688.2022.00045.
- [12] O. Ganea, G. Bécigneul, and T. Hofmann. Hyperbolic neural networks. In S. Bengio, H. Wallach, H. Larochelle, K. Grauman, N. Cesa-Bianchi, and R. Garnett, editors, *Advances in Neural Information Processing Systems*, volume 31. Curran Associates, Inc., 2018. URL <https://proceedings.neurips.cc/paper/2018/file/dbab2adc8f9d078009ee3fa810bea142-Paper.pdf>.
- [13] P. Ghosh, M. S. M. Sajjadi, A. Vergari, M. Black, and B. Schölkopf. From variational to deterministic autoencoders, 2019. URL <https://arxiv.org/abs/1903.12436>.
- [14] I. Goodfellow, J. Shlens, and C. Szegedy. Explaining and harnessing adversarial examples. In *International Conference on Learning Representations*, 2015. URL <http://arxiv.org/abs/1412.6572>.
- [15] J. Grosek. Fundamental reflection domains for hyperbolic tesselations. In *Rose-Hulman Undergraduate Mathematics Journal*, volume 9, 2008. URL <https://scholar.rose-hulman.edu/rhumj/vol9/iss1/4>.
- [16] Y. Guo, X. Wang, Y. Chen, and S. X. Yu. Clipped hyperbolic classifiers are super-hyperbolic classifiers. In *2022 IEEE/CVF Conference on Computer Vision and Pattern Recognition (CVPR)*, pages 1–10, Los Alamitos, CA, USA, jun 2022. IEEE Computer Society. doi: 10.1109/CVPR52688.2022.00010. URL <https://doi.ieeecomputersociety.org/10.1109/CVPR52688.2022.00010>.

[17] K. He, X. Zhang, S. Ren, and J. Sun. Delving deep into rectifiers: Surpassing human-level performance on imagenet classification. In *Proceedings of the IEEE International Conference on Computer Vision (ICCV)*, December 2015.

[18] K. He, X. Zhang, S. Ren, and J. Sun. Deep residual learning for image recognition. *CoRR*, abs/1512.03385, 2015. URL <http://arxiv.org/abs/1512.03385>.

[19] M. Heusel, H. Ramsauer, T. Unterthiner, B. Nessler, and S. Hochreiter. Gans trained by a two time-scale update rule converge to a local nash equilibrium. In *Proceedings of the 31st International Conference on Neural Information Processing Systems, NIPS'17*, page 6629–6640, Red Hook, NY, USA, 2017. Curran Associates Inc. ISBN 9781510860964.

[20] J. Hsu, J. Gu, G.-H. Wu, W. Chiu, and S. Yeung. Capturing implicit hierarchical structure in 3d biomedical images with self-supervised hyperbolic representations, 2020. URL <https://arxiv.org/abs/2012.01644>.

[21] S. Ioffe and C. Szegedy. Batch normalization: Accelerating deep network training by reducing internal covariate shift. In *Proceedings of the 32nd International Conference on International Conference on Machine Learning - Volume 37*, ICML'15, page 448–456. JMLR.org, 2015.

[22] V. Khrulkov, L. Mirvakhabova, E. Ustinova, I. Oseledets, and V. Lempitsky. Hyperbolic image embeddings. In *2020 IEEE/CVF Conference on Computer Vision and Pattern Recognition (CVPR)*, pages 6417–6427, Los Alamitos, CA, USA, jun 2020. IEEE Computer Society. doi: 10.1109/CVPR42600.2020.00645. URL <https://doi.ieee.org/10.1109/CVPR42600.2020.00645>.

[23] D. P. Kingma and M. Welling. Auto-encoding variational bayes, 2013. URL <https://arxiv.org/abs/1312.6114>.

[24] R. J. Kobler, J.-i. Hirayama, and M. Kawanabe. Controlling the fréchet variance improves batch normalization on the symmetric positive definite manifold. In *ICASSP 2022 - 2022 IEEE International Conference on Acoustics, Speech and Signal Processing (ICASSP)*, pages 3863–3867, 2022. doi: 10.1109/ICASSP43922.2022.9746629.

[25] M. Kochurov, R. Karimov, and S. Kozlukov. Geoopt: Riemannian optimization in pytorch, 2020.

[26] A. Krizhevsky. Learning multiple layers of features from tiny images. pages 32–33, 2009. URL <https://www.cs.toronto.edu/~kriz/learning-features-2009-TR.pdf>.

[27] M. Law, R. Liao, J. Snell, and R. Zemel. Lorentzian distance learning for hyperbolic representations. In K. Chaudhuri and R. Salakhutdinov, editors, *Proceedings of the 36th International Conference on Machine Learning*, volume 97 of *Proceedings of Machine Learning Research*, pages 3672–3681. PMLR, 09–15 Jun 2019. URL <https://proceedings.mlr.press/v97/law19a.html>.

[28] Y. Le and X. S. Yang. Tiny imagenet visual recognition challenge. 2015.

[29] G. Lebanon and J. Lafferty. Hyperplane margin classifiers on the multinomial manifold. In *Proceedings of the Twenty-First International Conference on Machine Learning, ICML '04*, page 66, New York, NY, USA, 2004. Association for Computing Machinery. ISBN 1581138385. doi: 10.1145/1015330.1015333. URL <https://doi.org/10.1145/1015330.1015333>.

[30] Y. Lecun, L. Bottou, Y. Bengio, and P. Haffner. Gradient-based learning applied to document recognition. *Proceedings of the IEEE*, 86(11):2278–2324, 1998. doi: 10.1109/5.726791.

[31] S. Liu, J. Chen, L. Pan, C.-W. Ngo, T.-S. Chua, and Y.-G. Jiang. Hyperbolic visual embedding learning for zero-shot recognition. In *2020 IEEE/CVF Conference on Computer Vision and Pattern Recognition (CVPR)*, pages 9270–9278, 2020. doi: 10.1109/CVPR42600.2020.00929.

[32] Z. Liu, P. Luo, X. Wang, and X. Tang. Deep learning face attributes in the wild. In *2015 IEEE International Conference on Computer Vision (ICCV)*, pages 3730–3738, 2015. doi: 10.1109/ICCV.2015.425.

[33] A. Lou, I. Katsman, Q. Jiang, S. Belongie, S.-N. Lim, and C. De Sa. Differentiating through the fréchet mean, 2020. URL <https://arxiv.org/abs/2003.00335>.

[34] A. Madry, A. Makelov, L. Schmidt, D. Tsipras, and A. Vladu. Towards deep learning models resistant to adversarial attacks, 2019.

[35] E. Mathieu, C. L. Lan, C. J. Maddison, R. Tomioka, and Y. W. Teh. Continuous hierarchical representations with poincaré variational auto-encoders, 2019. URL <https://arxiv.org/abs/1901.06033>.

[36] G. Mishne, Z. Wan, Y. Wang, and S. Yang. The numerical stability of hyperbolic representation learning, 2022. URL <https://arxiv.org/abs/2211.00181>.

[37] V. Moretti. The interplay of the polar decomposition theorem and the lorentz group, 2002. URL <https://arxiv.org/abs/math-ph/0211047>.

[38] Y. Nagano, S. Yamaguchi, Y. Fujita, and M. Koyama. A wrapped normal distribution on hyperbolic space for gradient-based learning, 2019. URL <https://arxiv.org/abs/1902.02992>.

[39] M. Nickel and D. Kiela. Learning continuous hierarchies in the lorentz model of hyperbolic geometry, 2018. URL <https://arxiv.org/abs/1806.03417>.

[40] I. Ovinnikov. Poincaré wasserstein autoencoder. 2019. doi: 10.48550/ARXIV.1901.01427. URL <https://arxiv.org/abs/1901.01427>.

[41] A. Paszke, S. Gross, F. Massa, A. Lerer, J. Bradbury, G. Chanan, T. Killeen, Z. Lin, N. Gimelshein, L. Antiga, A. Desmaison, A. Kopf, E. Yang, Z. DeVito, M. Raison, A. Tejani, S. Chilamkurthy, B. Steiner, L. Fang, J. Bai, and S. Chintala. Pytorch: An imperative style, high-performance deep learning library. In *Advances in Neural Information Processing Systems 32*, pages 8024–8035. Curran Associates, Inc., 2019. URL <http://papers.neurips.cc/paper/9015-pytorch-an-imperative-style-high-performance-deep-learning-library.pdf>.

[42] W. Peng, T. Varanka, A. Mostafa, H. Shi, and G. Zhao. Hyperbolic deep neural networks: A survey. *IEEE Transactions on Pattern Analysis and Machine Intelligence*, 44(12):10023–10044, 2022. doi: 10.1109/TPAMI.2021.3136921.

[43] X. Pennec. Intrinsic statistics on riemannian manifolds: Basic tools for geometric measurements. *Journal of Mathematical Imaging and Vision*, 25(1):127–154, 2006.

[44] E. Qu and D. Zou. Lorentzian fully hyperbolic generative adversarial network, 2022. URL <https://arxiv.org/abs/2201.12825>.

[45] J. G. Ratcliffe. *Foundations of Hyperbolic Manifolds*. Springer, 2 edition, 2006.

[46] D. J. Rezende, S. Mohamed, and D. Wierstra. Stochastic backpropagation and approximate inference in deep generative models, 2014. URL <https://arxiv.org/abs/1401.4082>.

[47] R. Sarkar. Low distortion delaunay embedding of trees in hyperbolic plane. In M. van Kreveld and B. Speckmann, editors, *Graph Drawing*, pages 355–366, Berlin, Heidelberg, 2012. Springer Berlin Heidelberg. ISBN 978-3-642-25878-7.

[48] M. Seitzer. pytorch-fid: FID Score for PyTorch. <https://github.com/mseitzer/pytorch-fid>, August 2020. Version 0.2.1.

[49] R. Shimizu, Y. Mukuta, and T. Harada. Hyperbolic neural networks++, 2020. URL <https://arxiv.org/abs/2006.08210>.

[50] T. Yu and C. M. De Sa. Numerically accurate hyperbolic embeddings using tiling-based models. In H. Wallach, H. Larochelle, A. Beygelzimer, F. d’Alch  -Buc, E. Fox, and R. Garnett, editors, *Advances in Neural Information Processing Systems*, volume 32. Curran Associates, Inc., 2019. URL <https://proceedings.neurips.cc/paper/2019/file/82c2559140b95ccda9c6ca4a8b981f1e-Paper.pdf>.

[51] Y. Yue, F. Lin, K. D. Yamada, and Z. Zhang. Hyperbolic contrastive learning, 2023. URL <https://arxiv.org/abs/2302.01409>.

[52] S. Zagoruyko and N. Komodakis. Wide residual networks, 2017.

[53] H. Zhang, P. D. Rich, A. K. Lee, and T. O. Sharpee. Hippocampal spatial representations exhibit a hyperbolic geometry that expands with experience. *Nature Neuroscience*, 26(1):131–139, 2023.

A Operations in hyperbolic geometry

A.1 Lorentz model

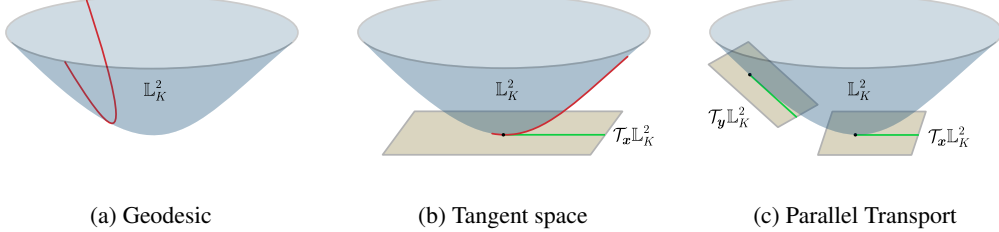


Figure 5: Illustrations of geometrical operations in the 2-dimensional Lorentz model. (a) The shortest distance between two points is represented by the connecting geodesic (red line). (b) The red line gets projected onto the tangent space of the origin resulting in the green line. (c) The green line gets parallel transported to the tangent space of the origin.

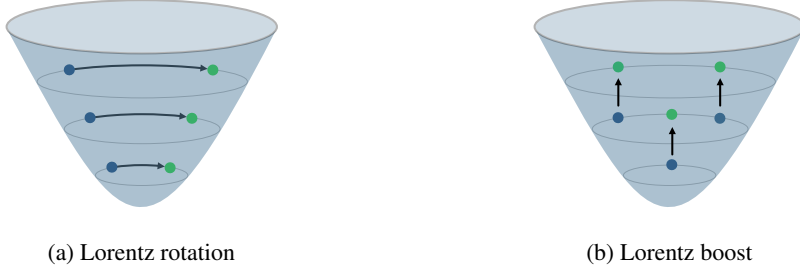


Figure 6: Illustration of the Lorentz transformations in the 2-dimensional Lorentz model.

In this section, we describe essential geometrical operations in the Lorentz model. Most of these operations are defined for all Riemannian manifolds and thus introduced for the general case first. However, the closed-form formulae are only given for the Lorentz model. We also provide visual illustrations in Figure 5.

Distance Distance is defined as the length of the shortest path between a pair of points on a surface. While in Euclidean geometry, this is a straight line, in hyperbolic space, the shortest path is represented by a curved geodesic generalizing the notion of a straight line. In the Lorentz model, the distance is inherited from Minkowski space. Let $\mathbf{x}, \mathbf{y} \in \mathbb{L}_K^n$ denote two points in the Lorentz model. Then, the length of the connecting geodesic and, thereby, the distance is given by

$$d_{\mathcal{L}}(\mathbf{x}, \mathbf{y}) = \frac{1}{\sqrt{-K}} \cosh^{-1}(K \langle \mathbf{x}, \mathbf{y} \rangle_{\mathcal{L}}), \quad (14)$$

and the squared distance [27] by

$$d_{\mathcal{L}}^2(\mathbf{x}, \mathbf{y}) = \|\mathbf{x} - \mathbf{y}\|_{\mathcal{L}}^2 = \frac{2}{K} - 2 \langle \mathbf{x}, \mathbf{y} \rangle_{\mathcal{L}}. \quad (15)$$

When calculating the distance of any point $\mathbf{x} \in \mathbb{L}_K^n$ to the origin $\bar{\mathbf{0}}$, the equations can be simplified to

$$d_{\mathcal{L}}(\mathbf{x}, \bar{\mathbf{0}}) = \|\log_{\bar{\mathbf{0}}}^K(\mathbf{x})\|, \quad (16)$$

$$d_{\mathcal{L}}^2(\mathbf{x}, \bar{\mathbf{0}}) = \frac{2}{K} (1 + \sqrt{-K} x_t). \quad (17)$$

Tangent space The space around each point \mathbf{x} on a differentiable manifold \mathcal{M} can be linearly approximated by the tangent space $\mathcal{T}_{\mathbf{x}}\mathcal{M}$. It is a first-order approximation bridging the gap to Euclidean space. This helps performing Euclidean operations, but it introduces an approximation error, which generally increases with the distance from the reference point. Let $\mathbf{x} \in \mathbb{L}_K^n$, then the tangent space at point \mathbf{x} can be expressed as

$$\mathcal{T}_{\mathbf{x}}\mathbb{L}_K^n := \{\mathbf{y} \in \mathbb{R}^{n+1} \mid \langle \mathbf{y}, \mathbf{x} \rangle_{\mathcal{L}} = 0\}. \quad (18)$$

Exponential and logarithmic maps Exponential and logarithmic maps are mappings between the manifold \mathcal{M} and the tangent space $\mathcal{T}_{\mathbf{x}}\mathcal{M}$ with $\mathbf{x} \in \mathcal{M}$. The exponential map $\exp_{\mathbf{x}}^K(\mathbf{z}) : \mathcal{T}_{\mathbf{x}}\mathbb{L}_K^n \rightarrow \mathbb{L}_K^n$ maps a tangent vector $\mathbf{z} \in \mathcal{T}_{\mathbf{x}}\mathbb{L}_K^n$ on the Lorentz manifold by

$$\exp_{\mathbf{x}}^K(\mathbf{z}) = \cosh(\alpha)\mathbf{x} + \sinh(\alpha)\frac{\mathbf{z}}{\alpha}, \text{ with } \alpha = \sqrt{-K}\|\mathbf{z}\|_{\mathcal{L}}, \quad \|\mathbf{z}\|_{\mathcal{L}} = \sqrt{\langle \mathbf{z}, \mathbf{z} \rangle_{\mathcal{L}}}. \quad (19)$$

The logarithmic map is the inverse mapping and maps a vector $\mathbf{y} \in \mathbb{L}_K^n$ to the tangent space of \mathbf{x} by

$$\log_{\mathbf{x}}^K(\mathbf{y}) = \frac{\cosh^{-1}(\beta)}{\sqrt{\beta^2 - 1}} \cdot (\mathbf{y} - \beta\mathbf{x}), \text{ with } \beta = K\langle \mathbf{x}, \mathbf{y} \rangle_{\mathcal{L}}. \quad (20)$$

In the special case of working with the tangent space at the origin $\bar{\mathbf{0}}$, the exponential map simplifies to

$$\exp_{\bar{\mathbf{0}}}^K(\mathbf{z}) = \frac{1}{\sqrt{-K}} \left[\cosh(\sqrt{-K}\|\mathbf{z}\|), \sinh(\sqrt{-K}\|\mathbf{z}\|) \frac{\mathbf{z}}{\|\mathbf{z}\|} \right]. \quad (21)$$

Parallel transport The parallel transport operation $\text{PT}_{\mathbf{x} \rightarrow \mathbf{y}}^K(\mathbf{v})$ maps a vector $\mathbf{v} \in \mathcal{T}_{\mathbf{x}}\mathcal{M}$ from the tangent space of $\mathbf{x} \in \mathcal{M}$ to the tangent space of $\mathbf{y} \in \mathcal{M}$. It preserves the local geometry around the reference point by moving the points along the geodesic connecting \mathbf{x} and \mathbf{y} . The formula for the Lorentz model is given by

$$\text{PT}_{\mathbf{x} \rightarrow \mathbf{y}}^K(\mathbf{v}) = \mathbf{v} - \frac{\langle \log_{\mathbf{x}}^K(\mathbf{y}), \mathbf{v} \rangle_{\mathcal{L}}}{d_{\mathcal{L}}(\mathbf{x}, \mathbf{y})} (\log_{\mathbf{x}}^K(\mathbf{y}) + \log_{\mathbf{y}}^K(\mathbf{x})) \quad (22)$$

$$= \mathbf{v} + \frac{\langle \mathbf{y}, \mathbf{v} \rangle_{\mathcal{L}}}{\frac{1}{-K} - \langle \mathbf{x}, \mathbf{y} \rangle_{\mathcal{L}}} (\mathbf{x} + \mathbf{y}). \quad (23)$$

Lorentzian centroid [27] The weighted centroid with respect to the squared Lorentzian distance, which solves $\min_{\boldsymbol{\mu} \in \mathbb{L}_K^n} \sum_{i=1}^m \nu_i d_{\mathcal{L}}^2(\mathbf{x}_i, \boldsymbol{\mu})$, with $\mathbf{x}_i \in \mathbb{L}_K^n$ and $\nu_i \geq 0$, $\sum_{i=1}^m \nu_i > 0$, is given by

$$\boldsymbol{\mu} = \frac{\sum_{i=1}^m \nu_i \mathbf{x}_i}{\sqrt{-K} \|\sum_{i=1}^m \nu_i \mathbf{x}_i\|_{\mathcal{L}}}. \quad (24)$$

Lorentz transformations The set of linear transformations in the Lorentz model are called Lorentz transformations. A transformation matrix $\mathbf{A}^{(n+1) \times (n+1)}$ that linearly maps $\mathbb{R}^{n+1} \rightarrow \mathbb{R}^{n+1}$ is called Lorentz transformation if and only if $\langle \mathbf{A}\mathbf{x}, \mathbf{A}\mathbf{y} \rangle_{\mathcal{L}} = \langle \mathbf{x}, \mathbf{y} \rangle_{\mathcal{L}} \forall \mathbf{x}, \mathbf{y} \in \mathbb{R}^{n+1}$. The set of matrices forms an orthogonal group $\mathbf{O}(1, n)$ called the Lorentz group. As the Lorentz model only uses the upper sheet of the two-sheeted hyperboloid, the transformations under consideration here lie within the positive Lorentz group $\mathbf{O}^+(1, n) = \{\mathbf{A} \in \mathbf{O}(1, n) : a_{11} > 0\}$, preserving the sign of the time component x_t of $\mathbf{x} \in \mathbb{L}_K^n$. Specifically, here, the Lorentz transformations can be formulated as

$$\mathbf{O}^+(1, n) = \{\mathbf{A} \in \mathbb{R}^{(n+1) \times (n+1)} \mid \forall \mathbf{x} \in \mathbb{L}_K^n : \langle \mathbf{A}\mathbf{x}, \mathbf{A}\mathbf{x} \rangle_{\mathcal{L}} = \frac{1}{K}, (\mathbf{A}\mathbf{x})_0 > 0\}. \quad (25)$$

Any Lorentz transformation can be decomposed into a Lorentz rotation and Lorentz boost by polar decomposition $\mathbf{A} = \mathbf{R}\mathbf{B}$ [37]. The former rotates points around the time axis, using matrices given by

$$\mathbf{R} = \begin{bmatrix} 1 & \mathbf{0}^T \\ \mathbf{0} & \tilde{\mathbf{R}} \end{bmatrix}, \quad (26)$$

where $\mathbf{0}$ is a zero vector, $\tilde{\mathbf{R}}^T \tilde{\mathbf{R}} = \mathbf{I}$, and $\det(\tilde{\mathbf{R}}) = 1$. This shows that the Lorentz rotations for the upper sheet lie in a special orthogonal subgroup $SO^+(1, n)$ preserving the orientation, while $\tilde{\mathbf{R}} \in SO(n)$. On the other side, the Lorentz boost moves points along the spatial axis given a velocity $\mathbf{v} \in \mathbb{R}^n$, $\|\mathbf{v}\| < 1$ without rotating them along the time axis. Formally, the boost matrices are given by

$$\mathbf{B} = \begin{bmatrix} \gamma & -\gamma \mathbf{v}^T \\ -\gamma \mathbf{v} & \mathbf{I} + \frac{\gamma^2}{1+\gamma} \mathbf{v} \mathbf{v}^T \end{bmatrix}, \quad (27)$$

with $\gamma = \frac{1}{\sqrt{1-\|\mathbf{v}\|^2}}$. See Figure 6 for illustrations of the Lorentz rotation and Lorentz boost.

Lorentz fully-connected layer Recently, Chen et al. [5] showed that the linear transformations performed in the tangent space [12, 39] can not apply all Lorentz transformations but only a special rotation and no boost. They proposed a direct method in pseudo-hyperbolic space², which can apply all Lorentz transformations. Specifically, let $\mathbf{x} \in \mathbb{L}_K^n$ denote the input vector and $\mathbf{W} \in \mathbb{R}^{m \times n+1}$, $\mathbf{v} \in \mathbb{R}^{n+1}$ the weight parameters, then the transformation matrix is given by

$$f_{\mathbf{x}}(\mathbf{M}) = f_{\mathbf{x}} \left(\begin{bmatrix} \mathbf{v}^T \\ \mathbf{W} \end{bmatrix} \right) = \begin{bmatrix} \sqrt{\|\mathbf{W}\mathbf{x}\|^2 - 1/K} \mathbf{v}^T \\ \mathbf{v}^T \mathbf{x} \\ \mathbf{W} \end{bmatrix}. \quad (28)$$

Adding other components of fully-connected layers, including normalization, the final definition of the proposed Lorentz fully-connected layer becomes

$$\mathbf{y} = \begin{bmatrix} \sqrt{\|\phi(\mathbf{W}\mathbf{x}, \mathbf{v})\|^2 - 1/K} \\ \phi(\mathbf{W}\mathbf{x}, \mathbf{v}) \end{bmatrix}, \quad (29)$$

with operation function

$$\phi(\mathbf{W}\mathbf{x}, \mathbf{v}) = \lambda \sigma(\mathbf{v}^T \mathbf{x} + \mathbf{b}') \frac{\mathbf{W}\psi(\mathbf{x}) + \mathbf{b}}{\|\mathbf{W}\psi(\mathbf{x}) + \mathbf{b}\|}, \quad (30)$$

where $\lambda > 0$ is a learnable scaling parameter and $\mathbf{b} \in \mathbb{R}^n$, ψ, σ denote the bias, activation, and sigmoid function, respectively.

In this work, we simplify the layer definition by removing the internal normalization, as we use batch normalization. This gives following formula for the Lorentz fully connected layer

$$\mathbf{y} = \text{LFC}(\mathbf{x}) = \begin{bmatrix} \sqrt{\|\psi(\mathbf{W}\mathbf{x} + \mathbf{b})\|^2 - 1/K} \\ \psi(\mathbf{W}\mathbf{x} + \mathbf{b}) \end{bmatrix}. \quad (31)$$

Lorentz direct concatenation [44] Given a set of hyperbolic points $\{\mathbf{x}_i \in \mathbb{L}_K^n\}_{i=1}^N$, the Lorentz direct concatenation is given by

$$\mathbf{y} = \text{HCat}(\{\mathbf{x}_i\}_{i=1}^N) = \left[\sqrt{\sum_{i=1}^N x_{i_t}^2 + \frac{N-1}{K}}, \mathbf{x}_{1_s}^T, \dots, \mathbf{x}_{N_s}^T \right]^T, \quad (32)$$

where $\mathbf{y} \in \mathbb{L}_K^{nN} \subset \mathbb{R}^{nN+1}$.

²Chen et al. [5] note that their general formula is not fully hyperbolic, but a relaxation in implementation, while the input and output are still guaranteed to lie in the Lorentz model.

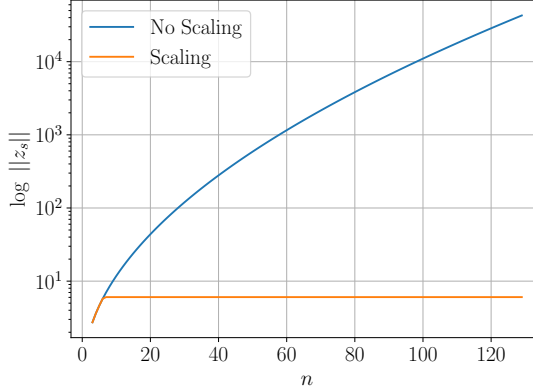


Figure 7: Growth of the space component's norm $\|z_s\|$ after applying the exponential map to an n -dimensional vector $\mathbf{1}_n = (1, \dots, 1) \in \mathcal{T}_{\mathbf{0}} \mathbb{L}_K^n$ with curvature $K = -1$. The y-axis is scaled logarithmically.

Wrapped normal distribution Nagano et al. [38] proposed a wrapped normal distribution in the Lorentz model, which offers efficient sampling, great flexibility, and a closed-form density formulation. It can be constructed as follows:

1. Sample a Euclidean vector $\tilde{\mathbf{v}}$ from the Normal distribution $\mathcal{N}(\mathbf{0}, \Sigma)$.
2. Assume the sampled vector lies in the tangent space of the Lorentz model's origin $\mathbf{v} = [0, \tilde{\mathbf{v}}] \in \mathcal{T}_{\mathbf{0}} \mathbb{L}_K^n$.
3. Parallel transport \mathbf{v} from the tangent space of the origin to the tangent space of a new mean $\boldsymbol{\mu} \in \mathbb{L}_K^n$, yielding a tangent vector $\mathbf{u} \in \mathcal{T}_{\boldsymbol{\mu}} \mathbb{L}_K^n$.
4. Map \mathbf{u} to \mathbb{L}_K^n by applying the exponential map, yielding the final sample $\mathbf{z} \in \mathbb{L}_K^n$.

The distribution is parameterized by a Euclidean variance $\Sigma \in \mathbb{R}^{n \times n}$ and a hyperbolic mean $\boldsymbol{\mu} \in \mathbb{L}_K^n$.

This method has shown to work well in hybrid HNN settings. However, in our fully hyperbolic VAE, high Euclidean variances destabilize the model. This is because, usually, the VAE's prior is set to a standard normal distribution with unit variance $\tilde{\mathbf{v}} \sim \mathcal{N}(\mathbf{0}, \mathbf{I})$. However, for high dimensional spaces, this leads to large values after the exponential map. That is why we propose to scale the prior variance as follows.

Let $\mathbf{v} \in \mathcal{T}_{\mathbf{0}} \mathbb{L}_K^n$ denote a vector in the tangent space of the origin. Then the space component of the hyperbolic vector $\mathbf{z} \in \mathbb{L}_K^n$ resulting from the exponential map is given by

$$z_s = (\exp_{\mathbf{0}}^K(\mathbf{v}))_s = \frac{1}{\sqrt{-K}} \sinh(\sqrt{-K} \|\mathbf{v}\|) \frac{\mathbf{v}}{\|\mathbf{v}\|}. \quad (33)$$

This shows that the norm of the space component depends on the sinh function, which grows approximately exponentially with the norm of the tangent vector ($\|z_s\| = \frac{1}{\sqrt{-K}} \sinh(\sqrt{-K} \|\mathbf{v}\|)$). The norm of the space component is important as it gets used to calculate the time component $z_t = \sqrt{\|\mathbf{z}_s\|^2 - 1/K}$, and it indicates how large the values of the hyperbolic points are. Now, assume an n -dimensional vector $\mathbf{1}_n = (1, \dots, 1) \in \mathcal{T}_{\mathbf{0}} \mathbb{L}_K^n$, resembling the diagonal of the covariance matrix. Applying the exponential map to such a vector leads to fast-growing values with respect to the dimensionality n because the norm of the tangent vector increases with n :

$$\|\mathbf{1}_n\| = \sqrt{\sum_{i=1}^n 1^2} = \sqrt{n}. \quad (34)$$

To work against this, we propose to clip the norm of the prior variance as follows

$$\boldsymbol{\sigma}^2 = \begin{cases} \frac{s}{\sqrt{n}} & \text{if } \sqrt{n} > s \\ \boldsymbol{\sigma}^2 & \text{otherwise} \end{cases}, \quad (35)$$

where s parameterizes the resulting norm. This achieves a clipped time component with respect to the dimensionality of $\mathbf{1}_n$ (see Figure 7). Furthermore, it offers nice interpretability using the Fréchet variance. As the distribution has zero mean, the Fréchet variance is given by the distance to the origin, which can be calculated by the norm of the tangent vector. This shows that this method controls the Fréchet variance. In practice, we empirically found $s = 2.5$ to be a good value.

Additionally, to prevent the HCNN-VAE from predicting relatively high variances, the scaling in Eq. 35 is applied. In this case, the Fréchet variance is not predefined, as usually $\boldsymbol{\sigma}^2 \neq \mathbf{1}_n$. However, it introduces a scaling operation resembling the variance scaling of the prior.

A.2 Mapping between models

Because of the isometry between models of hyperbolic geometry, points in the Lorentz model can be mapped to the Poincaré ball by the following diffeomorphism

$$p_{\mathbb{L}_K^n \rightarrow \mathbb{B}_K^n}(\mathbf{x}) = \frac{\mathbf{x}_s}{x_t + \frac{1}{\sqrt{-K}}}. \quad (36)$$

B Proofs

B.1 Proofs for Lorentz hyperplane

This section contains the proof for the Euclidean reparameterization of the Lorentz hyperplane proposed by Mishne et al. [36]. Unfortunately, the authors only provided proof for the unit Lorentz model, i.e., assuming a curvature of $K = -1$. However, in general, the curvature can be different as $K < 0$. That is why we reproduce their proof for the general case.

Proof for Eq. 8 Let $a \in \mathbb{R}$, $\mathbf{z} \in \mathbb{R}^n$, and $\bar{\mathbf{z}} \in \mathcal{T}_0 \mathbb{L}_K^n = [0, a\mathbf{z}/\|\mathbf{z}\|]$. Then, Mishne et al. [36] parameterize a point in the Lorentz model as follows

$$\mathbf{p} \in \mathbb{L}_K^n := \exp_{\bar{\mathbf{0}}} \left(a \frac{\mathbf{z}}{\|\mathbf{z}\|} \right) \quad (37)$$

$$= \left[\frac{1}{\sqrt{-K}} \cosh(\alpha), \sinh(\alpha) \frac{a \frac{\mathbf{z}}{\|\mathbf{z}\|}}{\alpha} \right]. \quad (38)$$

Now, with $\alpha = \sqrt{-K} \|a \frac{\mathbf{z}}{\|\mathbf{z}\|}\|_L = \sqrt{-K} a$ we get

$$\mathbf{p} = \left[\cosh(\sqrt{-K} a) \frac{1}{\sqrt{-K}}, \sinh(\sqrt{-K} a) \frac{a \frac{\mathbf{z}}{\|\mathbf{z}\|}}{\sqrt{-K}} \right] \quad (39)$$

$$= \frac{1}{\sqrt{-K}} \left[\cosh(\sqrt{-K} a), \sinh(\sqrt{-K} a) \frac{\mathbf{z}}{\|\mathbf{z}\|} \right]. \quad (40)$$

This definition gets used to reparameterize the hyperplane parameter \mathbf{w} as follows

$$\begin{aligned}
\mathbf{w} &:= \text{PT}_{\bar{\mathbf{0}} \rightarrow \mathbf{p}}^K(\bar{\mathbf{z}}) \\
&= \bar{\mathbf{z}} + \frac{\langle \mathbf{p}, \bar{\mathbf{z}} \rangle_{\mathcal{L}}}{\frac{1}{-K} - \langle \bar{\mathbf{0}}, \mathbf{p} \rangle_{\mathcal{L}}}(\bar{\mathbf{0}} + \mathbf{p}) \\
&= [0, \mathbf{z}]^T + \frac{\langle \mathbf{p}, [0, \mathbf{z}]^T \rangle_{\mathcal{L}}}{\frac{1}{-K} - \langle \bar{\mathbf{0}}, \mathbf{p} \rangle_{\mathcal{L}}}(\bar{\mathbf{0}} + \mathbf{p}) \\
&= [0, \mathbf{z}]^T + \frac{\frac{1}{\sqrt{-K}} \sinh(\sqrt{-K}a) \|\mathbf{z}\|}{\frac{1}{-K} + \frac{1}{-K} \cosh(\sqrt{-K}a)} \cdot \frac{1}{\sqrt{-K}} \left[1 + \cosh(\sqrt{-K}a), \sinh(\sqrt{-K}a) \frac{\mathbf{z}}{\|\mathbf{z}\|} \right] \\
&= [0, \mathbf{z}]^T + \frac{\sinh(\sqrt{-K}a) \|\mathbf{z}\|}{1 + \cosh(\sqrt{-K}a)} \cdot \left[1 + \cosh(\sqrt{-K}a), \sinh(\sqrt{-K}a) \frac{\mathbf{z}}{\|\mathbf{z}\|} \right] \\
&= \left[\sinh(\sqrt{-K}a) \|\mathbf{z}\|, \mathbf{z} + \frac{\sinh^2(\sqrt{-K}a)}{1 + \cosh(\sqrt{-K}a)} \mathbf{z} \right] \\
&= \left[\sinh(\sqrt{-K}a) \|\mathbf{z}\|, \mathbf{z} + \frac{\cosh^2(\sqrt{-K}a) - 1}{1 + \cosh(\sqrt{-K}a)} \mathbf{z} \right] \\
&= [\sinh(\sqrt{-K}a) \|\mathbf{z}\|, \cosh(\sqrt{-K}a) \mathbf{z}].
\end{aligned}$$

Proof for Eq. 9 After inserting Eq. 8 into Eq. 7 and solving the inner product, the hyperplane definition becomes

$$\tilde{H}_{\mathbf{z},a} = \{\mathbf{x} \in \mathbb{L}_K^n \mid \cosh(\sqrt{-K}a) \langle \mathbf{z}, \mathbf{x}_s \rangle - \sinh(\sqrt{-K}a) \|\mathbf{z}\| x_t = 0\}. \quad (41)$$

B.2 Proof for distance to Lorentz hyperplane

Proof for Theorem 1 To proof the distance of a point to hyperplanes in the Lorentz model, we follow the approach of Cho et al. [6] and utilize the hyperbolic reflection. The idea is, that a hyperplane defines a reflection that interchanges two half-spaces. Therefore, the distance from a point $\mathbf{x} \in \mathbb{L}_K^n$ to the hyperplane $H_{\mathbf{w},\mathbf{p}}$ can be calculated by halving the distance to its reflection in the hyperplane $\mathbf{x} \rightarrow \mathbf{y}_{\mathbf{w}}$

$$d_{\mathcal{L}}(\mathbf{x}, H_{\mathbf{w},\mathbf{p}}) = \frac{1}{2} d_{\mathcal{L}}(\mathbf{x}, \mathbf{y}_{\mathbf{w}}). \quad (42)$$

The hyperbolic reflection is well-known in the literature [15] and can be formulated as

$$\mathbf{y}_{\mathbf{w}} = \mathbf{x} + \frac{2\langle \mathbf{w}, \mathbf{x} \rangle_{\mathcal{L}} \mathbf{w}}{\langle \mathbf{w}, \mathbf{w} \rangle_{\mathcal{L}}}, \quad (43)$$

where \mathbf{w} is the perpendicular vector to the hyperplane and $\langle \mathbf{w}, \mathbf{w} \rangle_{\mathcal{L}} > 0$. Now, inserting Eq. 43 into Eq. 42 we can compute the distance to the hyperplane as follows

$$\begin{aligned}
d_{\mathcal{L}}(\mathbf{x}, H_{\mathbf{w}, \mathbf{p}}) &= \frac{1}{2\sqrt{-K}} \cosh^{-1}(K \langle \mathbf{x}, \mathbf{y}_{\mathbf{w}} \rangle_{\mathcal{L}}) \\
&= \frac{1}{2\sqrt{-K}} \cosh^{-1}(K \langle \mathbf{x}, \mathbf{x} + \frac{2\langle \mathbf{w}, \mathbf{x} \rangle_{\mathcal{L}} \mathbf{w}}{\langle \mathbf{w}, \mathbf{w} \rangle_{\mathcal{L}}} \rangle_{\mathcal{L}}) \\
&= \frac{1}{2\sqrt{-K}} \cosh^{-1}(2K \langle \mathbf{x}, \mathbf{x} \rangle_{\mathcal{L}} + K \langle \mathbf{x}, \frac{\langle \mathbf{w}, \mathbf{x} \rangle_{\mathcal{L}} \mathbf{w}}{\langle \mathbf{w}, \mathbf{w} \rangle_{\mathcal{L}}} \rangle_{\mathcal{L}}) \\
&= \frac{1}{2\sqrt{-K}} \cosh^{-1} \left(K \frac{1}{K} + 2K \left(\frac{\langle \mathbf{w}, \mathbf{x} \rangle_{\mathcal{L}}}{\sqrt{\langle \mathbf{w}, \mathbf{w} \rangle_{\mathcal{L}}}} \right)^2 \right) \\
&= \frac{1}{2\sqrt{-K}} \cosh^{-1} \left(1 + 2 \left(\sqrt{-K} \frac{\langle \mathbf{w}, \mathbf{x} \rangle_{\mathcal{L}}}{\sqrt{\langle \mathbf{w}, \mathbf{w} \rangle_{\mathcal{L}}}} \right)^2 \right) \\
&= \frac{1}{\sqrt{-K}} \left| \sinh^{-1} \left(\sqrt{-K} \frac{\langle \mathbf{w}, \mathbf{x} \rangle_{\mathcal{L}}}{\|\mathbf{w}\|_{\mathcal{L}}} \right) \right|,
\end{aligned}$$

which gives the final formula:

$$d_{\mathcal{L}}(\mathbf{x}, H_{\mathbf{w}, \mathbf{p}}) = \frac{1}{\sqrt{-K}} \left| \sinh^{-1} \left(\sqrt{-K} \frac{\langle \mathbf{w}, \mathbf{x} \rangle_{\mathcal{L}}}{\|\mathbf{w}\|_{\mathcal{L}}} \right) \right|. \quad (44)$$

Comparing Eq. 44 to the equation of Cho et al. [6] shows that the distance formula for hyperplanes in the unit Lorentz model can be extended easily to the general case by inserting the curvature parameter K at two places.

Finally, defining \mathbf{w} with the aforementioned reparameterization

$$\mathbf{w} := \text{PT}_{\bar{0} \rightarrow \mathbf{p}}^K(\bar{\mathbf{z}}) = [\sinh(\sqrt{-K}a)\|\mathbf{z}\|, \cosh(\sqrt{-K}a)\mathbf{z}], \quad (45)$$

and solving the inner products, gives our final distance formula

$$d_{\mathcal{L}}(\mathbf{x}, \tilde{H}_{\mathbf{z}, a}) = \frac{1}{\sqrt{-K}} \left| \sinh^{-1} \left(\sqrt{-K} \frac{\cosh(\sqrt{-K}a) \langle \mathbf{z}, \mathbf{x}_s \rangle - \sinh(\sqrt{-K}a) \|\mathbf{z}\| x_t}{\sqrt{\|\cosh(\sqrt{-K}a)\mathbf{z}\|^2 - (\sinh(\sqrt{-K}a)\|\mathbf{z}\|)^2}} \right) \right|. \quad (46)$$

B.3 Proof for logits in the Lorentz MLR classifier

Proof for Theorem 2 Following Lebanon and Lafferty [29], given input $\mathbf{x} \in \mathbb{R}^n$ and C classes, the Euclidean MLR logits of class $c \in \{1, \dots, C\}$ can be expressed as

$$v_{\mathbf{w}_c}(\mathbf{x}) = \text{sign}(\langle \mathbf{w}_c, \mathbf{x} \rangle) \|\mathbf{w}_c\| d(\mathbf{x}, H_{\mathbf{w}_c}), \quad \mathbf{w}_c \in \mathbb{R}^n, \quad (47)$$

where $H_{\mathbf{w}_c}$ is the decision hyperplane of class c .

Replacing the Euclidean operations with their counterparts in the Lorentz model yields logits of class c for $\mathbf{x} \in \mathbb{L}_K^n$ as follows

$$v_{\mathbf{w}_c, \mathbf{p}_c}(\mathbf{x}) = \text{sign}(\langle \mathbf{w}_c, \mathbf{x} \rangle_{\mathcal{L}}) \|\mathbf{w}_c\|_{\mathcal{L}} d_{\mathcal{L}}(\mathbf{x}, H_{\mathbf{w}_c, \mathbf{p}_c}), \quad (48)$$

with $\mathbf{w}_c \in \mathcal{T}_{\mathbf{p}_c} \mathbb{L}_K^n$, $\mathbf{p}_c \in \mathbb{L}_K^n$, and $\langle \mathbf{w}_c, \mathbf{w}_c \rangle_{\mathcal{L}} > 0$.

Inserting Eq. 44 into Eq. 48 gives a general formula without our reparameterization

$$v_{\mathbf{w}_c, \mathbf{p}_c}(\mathbf{x}) = \frac{1}{\sqrt{-K}} \text{sign}(\langle \mathbf{w}_c, \mathbf{x} \rangle_{\mathcal{L}}) \|\mathbf{w}_c\|_{\mathcal{L}} \left| \sinh^{-1} \left(\sqrt{-K} \frac{\langle \mathbf{w}_c, \mathbf{x} \rangle_{\mathcal{L}}}{\|\mathbf{w}_c\|_{\mathcal{L}}} \right) \right|. \quad (49)$$

Now, we reparameterize \mathbf{w} with Eq. 45 again, which gives

$$\alpha := \langle \mathbf{w}_c, \mathbf{x} \rangle_{\mathcal{L}} = \cosh(\sqrt{-K}a) \langle \mathbf{z}, \mathbf{x}_s \rangle - \sinh(\sqrt{-K}a), \quad (50)$$

$$\beta := \|\mathbf{w}_c\|_{\mathcal{L}} = \sqrt{\|\cosh(\sqrt{-K}a)\mathbf{z}\|^2 - (\sinh(\sqrt{-K}a)\|\mathbf{z}\|)^2}, \quad (51)$$

with $a \in \mathbb{R}$ and $\mathbf{z} \in \mathbb{R}^n$. Finally, we obtain the equation in Theorem 2:

$$v_{\mathbf{z}_c, a_c}(\mathbf{x}) = \frac{1}{\sqrt{-K}} \operatorname{sign}(\alpha) \beta \left| \sinh^{-1} \left(\sqrt{-K} \frac{\alpha}{\beta} \right) \right|. \quad (52)$$

C Additional experimental details

C.1 Classification

Datasets For classification, we employ the benchmark datasets CIFAR-10 [26], CIFAR-100 [26], and Tiny-ImageNet [28]. The CIFAR-10 and CIFAR-100 datasets each contain 60,000 32 \times 32 colored images from 10 and 100 different classes, respectively. We use the dataset split implemented in PyTorch, which includes 50,000 training images and 10,000 testing images. Tiny-ImageNet is a small subset of the ImageNet [7] dataset, with 100,000 images of 200 classes downsized to 64 \times 64. Here, we use the official validation split for testing our models.

Settings Table 4 summarizes the hyperparameters we adopt from DeVries and Taylor [8] to train all classification models. Additionally, we use standard data augmentation methods in training, i.e., random mirroring and cropping. Regarding the feature clipping in hybrid HNNs, we tune the feature clipping parameter r between 0.8 and 5.0 and find that, for most experiments, the best feature clipping parameter is $r = 1$. Only the Lorentz hybrid ResNet performs best with $r = 4$ on Tiny-ImageNet, and $r = 2$ on CIFAR-100 with lower embedding dimensions. Overall, we observe that the hybrid Lorentz ResNet has fewer gradient issues, allowing for higher clipping values. The HCNN-ResNet does not need tuning of any additional hyperparameters.

Table 4: Summary of hyperparameters used in training classification models.

Hyperparameter	Value
Epochs	200
Batch size	128
Learning rate (LR)	1e-1
Drop LR epochs	60, 120, 160
Drop LR gamma	0.2
Weight decay	5e-4
Optimizer	(Riemannian)SGD
Floating point precision	32 bit
GPU type	RTX A5000
Num. GPUs	1 or 2
Hyperbolic curvature K	-1

C.2 Generation

Datasets For image generation, we use the aforementioned CIFAR-10 [26] and CIFAR-100 [26] datasets again. Additionally, we employ the CelebA [32] dataset, which includes colored 64 \times 64 images of human faces. Here, we use the PyTorch implementation, containing 162,770 training images, 19,867 validation images, and 19,962 testing images.

Settings For hyperbolic and Euclidean models, we use the same architecture (see Table 5) and training hyperparameters (see Table 6). We employ a vanilla VAE similar to Ghosh et al. [13] as the baseline Euclidean architecture (E-VAE). For the hybrid model, we replace the latent distribution of the E-VAE with the hyperbolic wrapped normal distribution in the Lorentz model [38] and the Poincaré ball [35], respectively. Replacing all layers with our proposed hyperbolic counterparts yields the fully hyperbolic model. Here, we include the variance scaling mentioned in Section A.1, as otherwise training fails with NaN errors. Furthermore, we set the curvature K for the Lorentz model to -1 and for the Poincaré ball to -0.1 .

We evaluate the VAEs by employing two versions of the FID [19] implemented by Seitzer [48]:

1. The *reconstruction FID* gives a lower bound on the generation quality. It is calculated by comparing test images with reconstructed validation images. As the CIFAR datasets have no official validation set, we exclude a fixed random portion of 10,000 images from the training set.
2. The *generation FID* measures the generation quality by comparing random generations from the models' latent space with the test set.

Table 5: Vanilla VAE architecture employed in all image generation experiments. Convolutional layers have a kernel size of 3×3 and transposed convolutional layers of 4×4 . s and p denote stride and zero padding, respectively. The MLR in the Euclidean model is mimicked by a 1×1 convolutional layer.

Layer	CIFAR-10/100	CelebA
ENCODER:		
$\rightarrow \text{PROJ}_{\mathbb{R}^n \rightarrow \mathbb{L}_K^n}$	$32 \times 32 \times 3$	$64 \times 64 \times 3$
$\rightarrow \text{CONV}_{64,s2,p1} \rightarrow \text{BN} \rightarrow \text{RELU}$	$16 \times 16 \times 64$	$32 \times 32 \times 64$
$\rightarrow \text{CONV}_{128,s2,p1} \rightarrow \text{BN} \rightarrow \text{RELU}$	$8 \times 8 \times 128$	$16 \times 16 \times 128$
$\rightarrow \text{CONV}_{256,s2,p1} \rightarrow \text{BN} \rightarrow \text{RELU}$	$4 \times 4 \times 256$	$8 \times 8 \times 256$
$\rightarrow \text{CONV}_{512,s2,p1} \rightarrow \text{BN} \rightarrow \text{RELU}$	$2 \times 2 \times 512$	$4 \times 4 \times 512$
$\rightarrow \text{FLATTEN}$	2048	8192
$\rightarrow \text{FC-MEAN}_d$	128	64
$\rightarrow \text{FC-VAR}_d \rightarrow \text{SOFTPLUS}$	128	64
DECODER:		
$\rightarrow \text{SAMPLE}$	128	64
$\rightarrow \text{FC}_{32768} \rightarrow \text{BN} \rightarrow \text{RELU}$	32768	32768
$\rightarrow \text{RESHAPE}$	$8 \times 8 \times 512$	$8 \times 8 \times 512$
$\rightarrow \text{CONVTR}_{256,s2,p1} \rightarrow \text{BN} \rightarrow \text{RELU}$	$16 \times 16 \times 256$	$16 \times 16 \times 256$
$\rightarrow \text{CONVTR}_{128,s2,p1} \rightarrow \text{BN} \rightarrow \text{RELU}$	$32 \times 32 \times 128$	$32 \times 32 \times 128$
$\rightarrow \text{CONVTR}_{64,s2,p1} \rightarrow \text{BN} \rightarrow \text{RELU}$	-	$64 \times 64 \times 64$
$\rightarrow \text{CONV}_{64,s1,p1}$	$32 \times 32 \times 64$	$64 \times 64 \times 64$
$\rightarrow \text{MLR}$	$32 \times 32 \times 3$	$64 \times 64 \times 3$

Table 6: Summary of hyperparameters used in training image generation models.

Hyperparameter	MNIST	CIFAR-10/100	CELEBA
Epochs	100	100	70
Batch size	100	100	100
Learning rate	5e-4	5e-4	5e-4
Weight decay	0	0	0
KL loss weight	0.312	0.024	0.09
Optimizer	(Riem)Adam	(Riem)Adam	(Riem)Adam
Floating point precision	32 bit	32 bit	32 bit
GPU type	RTX A5000	RTX A5000	RTX A5000
Num. GPUs	1	1	2

D Ablation experiments

In this section, we perform ablation studies to obtain additional insights into our proposed HCNN components. All ablation experiments consider image classification on CIFAR-100 using ResNet-18. We estimate the mean and standard deviation from five runs, and the best performance is highlighted in bold.

Runtime Currently, two major drawbacks of HNNs are relatively high runtime and memory requirements. This is partly due to custom Pythonic implementations of hyperbolic network components introducing significant computational overhead. To study the overhead in practice and assess the efficiency of our implementations, we use PyTorch’s *compile* function, which automatically builds a more efficient computation graph. We compare the runtime of our Lorentz ResNets with the Euclidean baseline under compiled and default settings in Table 7 using an RTX 4090 GPU.

The results show that hybrid HNNs only add little overhead compared to the significantly slower HCNN. This makes scaling HCNNs challenging and requires special attention in future works. However, we also see that hyperbolic models gain much more performance from the automatic compilation than the Euclidean model. This indicates greater room for improvement in terms of implementation optimizations.

Batch normalization In this experiment, we investigate the effectiveness of our proposed Lorentz batch normalization (LBN) compared to other possible methods. Specifically, we train HCNN-ResNets with different normalization methods and compare them against a model without normalization. The results are shown in Table 8.

Firstly, the batch normalization in tangent space and the Riemannian batch normalization [33] lead to infinite loss within the first few training iterations. This could be caused by the float32 precision used in this work. Additionally, the normalization within the Lorentz fully-connected layer (LFC) proposed by Chen et al. [5] (see Section A.1) inhibits learning when not combined with our LBN.

Conversely, using LBN alone improves convergence speed and accuracy significantly, getting approximately 36% higher accuracy than the non-normalized model after 200 epochs. Combining LBN and the LFC normalization leads to worse accuracy and runtime, validating our modified LFC (see Section A.1). Overall, this experiment shows the effectiveness of our LBN and suggests that, currently, there is no viable alternative for HNNs using the Lorentz model.

Non-linear activation In this work, we propose a method for applying standard activation functions to points in the Lorentz model that is more stable and efficient than the usual tangent space activations. Here, we quantify the improvement by comparing HCNN-ResNets using different ReLU applications. Furthermore, we consider a model without activation functions, as the LFC is non-linear already and might not need such functions.

The results in Table 9 show that non-linear activations improve accuracy significantly and are therefore needed in HCNNs. Furthermore, compared to Tangent ReLU, our Lorentz ReLU increases the average accuracy by 0.64%, decreases the runtime of a training epoch by about 16.7%, and is more consistent overall.

Table 7: Runtime improvement using PyTorch’s *compile* function on ResNet-18. Duration of a training epoch in seconds.

	Euclidean	Hybrid L.	HCNN
Default	7.4	9.2	103.3
Compiled	7.1	8.0	62.1
Difference	-4.1%	-13.0%	-39.9%

Table 8: Normalization ablation.

Normalization	Accuracy (%)
None	42.24 ± 3.86
Tangent bnorm	NaN
Riemannian bnorm [33]	NaN
LFC norm [5]	1.00 ± 0.00
LBN + LFC norm [5]	76.98 ± 0.18
LBN	78.07 ± 0.21

Table 9: Activation ablation.

Activation	Accuracy (%)
None	52.85 ± 0.41
Tangent ReLU	77.43 ± 0.45
Lorentz ReLU	78.07 ± 0.21

Residual connection In this experiment, we compare the effect of different approaches for residual connections on performance. As mentioned in Section 4.4, vector addition is ill-defined in the Lorentz model. As alternatives, we test tangent space addition [39], parallel transport (PT) addition [4], Möbius addition (after projecting to the Poincaré ball) [12], fully-connected (FC) layer addition [5], and our proposed space component addition. The results are shown in Table 10.

In training, we observe that PT and Möbius addition make the model very unstable, causing an early failure in the training process. This might be because of the float32 precision again. The tangent space addition performs relatively well, but the needed exponential and logarithmic maps add computational overhead ($\approx 12\%$ higher runtime per training epoch) and some instability that hampers learning. The FC addition and our proposed space addition are very similar and perform best. However, our method is simpler and therefore preferred.

Initialization Chen et al. [5] propose initializing Lorentz fully-connected layers with the uniform distribution $\mathcal{U}(-0.02, 0.02)$. As the LFC is the backbone of our Lorentz convolutional layer, we test the uniform initialization in HCNNs and compare it to the standard Kaiming initialization [17] used in most Euclidean CNNs. For this, we employ the same ResNet architecture and initialize Lorentz convolutional layers with these two methods.

The results in Table 11 show that the Kaiming initialization is preferred in HCNNs, leading to 0.55% higher accuracy.

Table 10: Residual connection ablation.

Residual connection	Accuracy (%)
Tangent addition [39]	77.73 ± 0.32
PT addition [4]	NaN
Möbius addition [12]	NaN
FC addition [5]	77.93 ± 0.25
Space addition	78.07 ± 0.21

Table 11: Initialization ablation.

Initialization	Accuracy (%)
$\mathcal{U}(-0.02, 0.02)$ [5]	77.52 ± 0.10
Kaiming [17]	78.07 ± 0.21